Available online at www.sciencedirect.com

ScienceDirect

journal homepage: www.elsevier.com/locate/he

Predominated capacitive behavior of Ag-doped magnesium vanadate as a novel electrode material for supercapacitors

Muhammad Umair [a], *Naveed Akhtar Shad* [b], *S. Hussain* [c], *Asim Jilani* [d], *Muhammad Munir Sajid* [e], *Muhammad Imran Arshad* [f], *Hafiz Talha Hasnain Rana* [a], *Surender Kumar Sharma* [g], *Yogendra Kumar Mishra* [h], *Yasir Javed* [a,*]

[a] *Department of Physics, University of Agriculture, Faisalabad, Pakistan*
[b] *National Institute of Biotechnology and Genetic Engineering, Jhang Road, Faisalabad, Pakistan*
[c] *Department of Physics, Division of Science and Technology, University of Education Lahore, Pakistan*
[d] *Center of Nanotechnology, King Abdul-Aziz University, Jeddah, 21589, Saudi Arabia*
[e] *Henan Key Laboratory of Photovoltaic Materials, School of Physics, Henan Normal University, Xinxiang, 453007, China*
[f] *Department of Physics, Government College University Faisalabad, Faisalabad, Pakistan*
[g] *Department of Physics, Central University of Punjab, Bathinda, 151104, Punjab, India*
[h] *Mads Clausen Institute, Nano SYD, University of Southern Denmark, Sønderborg, 6400, Denmark*

HIGHLIGHTS

- Phase and lattice parameters of zinc vanadate are changed due to difference in ionic radii of dopant element (Ag).
- Variable oxidation of states of vanadium are observed which cause improvement in electrochemical response.
- Ag (2%) doped magnesium vanadate shows higher specific capacitance (Cs = 706 Fg^{-1}) than undoped (325 Fg^{-1}).
- Silver-modified electrode exhibits energy density and power density of 65.5 $Whkg^{-1}$ and 12,100 Wkg^{-1} respectively.

GRAPHICAL ABSTRACT

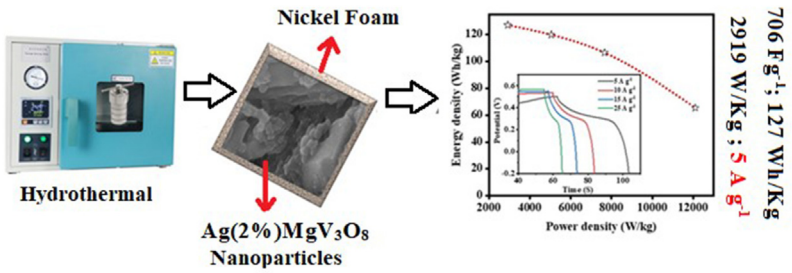

* *Corresponding author.*
E-mail address: myasi60@hotmail.com (Y. Javed).

https://doi.org/10.1016/j.ijhydene.2023.05.279

Please cite this article as: Umair M et al., Predominated capacitive behavior of Ag-doped magnesium vanadate as a novel electrode material for supercapacitors, International Journal of Hydrogen Energy, https://doi.org/10.1016/j.ijhydene.2023.05.279

ARTICLE INFO

Article history:
Received 26 February 2023
Received in revised form
22 May 2023
Accepted 26 May 2023
Available online xxx

Keywords:
Silver doped magnesium vanadate
Electrochemical properties
Surface-controlled process

ABSTRACT

Transition metal vanadate nanostructures are getting significant importance as an efficient electrode material for modern energy storage applications. In this work, a simple hydrothermal method is employed for the synthesis of magnesium vanadate (MgV_2O_5) and Ag-doped magnesium vanadate (Ag doped MgV_3O_8) nanomaterials. The X-ray diffraction (XRD) analysis reveals the formation of an orthorhombic structure for magnesium vanadate, whereas the Ag-doped magnesium vanadate results in a monoclinic structure. Interestingly, the optical bandgap is observed to increase from 2.85 eV to 3.92 eV with the increase in Ag-doping as revealed from Tauc's plot of the UV-visible absorption spectrum. The electrochemical performance of magnesium vanadate electrodes is thoroughly investigated by cyclic voltammetry (CV), Galvanostatic charge-discharge (GCD), and electrochemical impedance spectroscopy. The Ag-doped magnesium vanadate shows higher specific capacitance (C_s = 706 Fg^{-1}) in comparison to undoped (325 $Fg^{-1)}$ at a current density J = 5 Ag^{-1}. The theoretical investigations through Dunn's model demonstrate a major contribution arises from surface-controlled processes, which increase as high as 91% at scan rate of 60 $mVsec^{-1}$. Our findings indicate that Ag-doping significantly improves the overall electrochemical response of magnesium vanadate as an efficient electrode material for supercapacitor applications.

Introduction

Industrial and population growth led to massive use of fossil fuels, culminating in the gradual degradation of their sources [1]. This ultimate increase in the population has triggered an energy problem all over the world [2–4]. Researchers are paying very close attention to eco-friendly energy transformation and storage systems [5–10]. Electrochemical energy storage mechanizations have now leading and playing an attractive role in the worldwide efforts to solve the issues of sustainable energy production. Over the last two decades, enormous work has been reported for both rechargeable batteries and electrochemical capacitors development; however, both are still inadequate in terms of fossil fuel usage [11].

Supercapacitors are notable for their remarkable energy storage features, which include superior capacity, high power density, rapid charge/discharge mechanisms and longer cyclic stability. The supercapacitor can be divided into two categories i.e. Pseudo-capacitors and electrical double-layer capacitors depending on the charge storage process. Electrical charges can store in supercapacitors by two mechanisms i.e., faradaic (pseudo) or non-faradic (double-layer) reactions. Supercapacitors have the potential to be used as power sources in hybrid vehicles and mobile electronic gadgets in the future [12].

The choice of electrode material is essential in determining the electrical behavior of supercapacitors. Transition metals that have tunable valence states may give excellent pseudo capacitance. Metal compounds should possess three qualities to be a candidate as an electrode material; i.e., high conductivity, multiple valence states, and the proton intercalation into the lattice [13]. Due to its remarkable specific capacitance and strong conductivity, vanadium-based materials are considered important for supercapacitors. In the field of energy storage systems, V_2O_5 played a crucial role. The multiple oxidation states, higher specific capacitance, greater energy density, and proper cycle stability, with a novel layered structure, V_2O_5 is well-suitable [10,13,14]. Alkali earth metals exhibits two valence electron and superior electrical conductivity. Many alkali earth metal vanadium oxides, AV_xO_y (A = Mg, Ca.), have been used in rechargeable batteries such as (zinc, lithium, sodium, and magnesium ion batteries) [15–19]. However, from the perspective of supercapacitors, the exploration of alkali earth metals vanadium-based nanomaterials is less explored and neglected. Xu et al. (2020) reported that Mg could be adopted to achieve a higher capacity because it has a lower molecular mass than Ca, Sr, Ba, and Ra [20].

Metal doping is a potential approach for improving the electrical, optical, and electrochemical properties of magnesium Vanadate [21]. There are several doping materials (Cu, Nb, Zn, and Ag) but silver has been chosen due to simple link matrix nature and activity towards surface states in the nanostructures [22]. Additionally, silver doping can tailor the crystal structure of magnesium vanadate. To improve, the charge and discharge capacity of the batteries, silver is also reported in the literature. For example, Liang et al. (2013) fabricated $Ag/AgVO_3$ nanorods for lithium-ion batteries that exhibited a high specific capacity of 242 mA hg^{-1} at a current density of 50 mAg^{-1} and Li et al. (2016) synthesized multi-scale $AgVO_3$ particles for electrochemical performance and showed high capacity 243 mA hg^{-1} at current density of 1 Ag^{-1} [23,24].

To overcome the above gap, herein, we synthesized the magnesium vanadate and silver (1%, 1.5%, 2%) doped magnesium vanadate nanomaterials by using the hydrothermal method. X-ray diffraction analysis determines the orthorhombic and monoclinic crystal structure of undoped and doped magnesium vanadate respectively. Other materials related properties are investigated by SEM, EDX, UV–Vis spectroscopy, FTIR and XPS techniques. The electrochemical response of magnesium vanadate and silver-doped magnesium vanadate modified electrodes was also evaluated.

Please cite this article as: Umair M et al., Predominated capacitive behavior of Ag-doped magnesium vanadate as a novel electrode material for supercapacitors, International Journal of Hydrogen Energy, https://doi.org/10.1016/j.ijhydene.2023.05.279

Experimental

Chemicals

Magnesium nitrate (Mg $(NO_3)_2 \cdot 6H_2O$) (Daejung, 98%), Ammonium metavanadate (NH_4VO_3) (Daejung, 99%), Silver nitrate ($AgNO_3$) (Daejung, 99.8%), Sodium hydroxide (NaOH) (Sigma Aldrich, 97%), and Cetyltri methyl ammonium bromide (CTAB) (Glentham life sciences, 99%). No additional purification was performed to use any of the chemicals.

Synthesis protocol

Magnesium vanadate and silver (1%, 1.5%, 2%) doped magnesium vanadate nanoparticles were synthesized by using the hydrothermal method. In the typical synthesis of magnesium vanadate, 0.5 mol of Mg $(NO_3)_2 \cdot 6H_2O$ (12.82 g) and NH_4VO_3 (5.84 g) were dissolved in 100 ml distilled water separately. The two prepared solutions were mixed and stirred for 30 min. 0.2 g CTAB was added into the solution mixture as a stabilizing agent. The 0.5 M NaOH (2 g) solution was added dropwise into the mixture to maintain the pH between 10 and 12 and stirred for 1 h. This final mixture was shifted into a 100 ml Teflon-lined autoclave and put into the oven for 14 h at 180 °C for hydrothermal treatment. The autoclaves were cooled at room temperature after the hydrothermal process and the obtained suspension was centrifuged and washed three times with distilled water. The obtained precipitates were dried at 60 °C in an oven overnight and ground to form magnesium vanadate powder. The silver-doped magnesium vanadate nanomaterials were prepared by adding molar ratio of silver nitrate as 1% (0.16 g), 1.5% (0.25 g), and 2% (0.33 g) in the magnesium nitrate and ammonium vanadate solution, followed by the above-mentioned process. The schematic flow chart of different steps involved in the hydrothermal synthesis process is given in Fig. 1.

Characterization tools

X-ray diffraction analysis employing X-ray diffractometer with a Cu-Kα beam ($\lambda = 0.15406$ nm) revealed the crystalline nature of the synthesized nanomaterials. The surface morphology of synthesized nanomaterials was examined by using Nova Nano SEM. Fourier transform infrared spectroscopy was used to investigate functional groups of the synthesized nanomaterials using a (Cary-630) FTIR spectrophotometer. A UV-Vis spectrometer (T80) (200–900 nm range) was used to evaluate the optical properties of synthesized nanomaterials.

Electrochemical studies

The electrochemical response of magnesium vanadate and silver (2%) doped magnesium vanadate electrodes were analyzed by using a three-electrode assembly. 1 M KOH solution was utilized as an electrolyte. In a three-electrode system, one worked as a counter electrode, the second as a reference electrode, and the nanomaterials modified Ni foam as a working electrode. The working electrode was fabricated by using the weight percentage (10:10:80%) of polyvinyl alcohol (PVA), graphite, and synthesized material respectively [25–28]. The synthesized slurry was coated on 2×2 cm^2 nickel foam and dried. The deposited mass of the electrode was $\geq$2 mg.

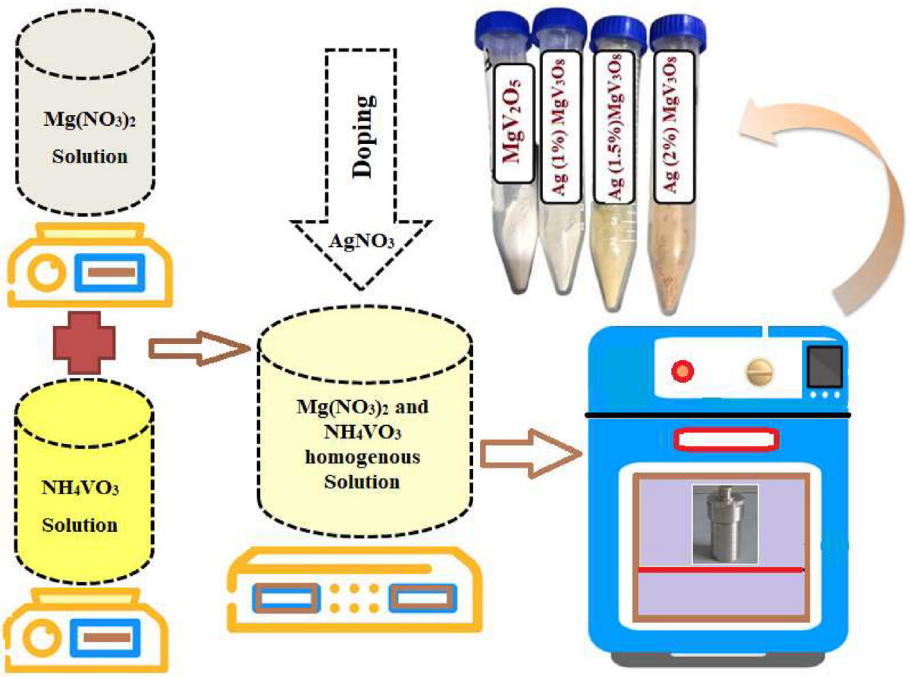

Fig. 1 – Flow chart of different steps involved in the synthesis process.

Please cite this article as: Umair M et al., Predominated capacitive behavior of Ag-doped magnesium vanadate as a novel electrode material for supercapacitors, International Journal of Hydrogen Energy, https://doi.org/10.1016/j.ijhydene.2023.05.279

Results and discussion

Materials' characterization

Fig. 2a shows the XRD spectra of as-synthesized magnesium vanadate and silver (1.0%, 1.5%, 2.0%) doped magnesium vanadate. In case of magnesium vanadate, all the diffraction peaks are correlated well with JCPDS card number 00-030-0801 with an orthorhombic crystal structure and space group $Cmc2_1$. The chemical formula for related magnesium vanadate observed from the JCPDS card is MgV_2O_5. The diffraction peaks present at $2\theta = 34.5°$, 36.2°, 42.5°, 56.8°, 60.6°, and 62.7° correspond to (113), (130), (114), (116), (204), and (154) planes, respectively. After Ag doping, the XRD patterns reveal the phase transformation of magnesium vanadate from MgV_2O_5 to MgV_3O_8 as diffraction peaks in magnesium vanadate with different Ag doping are matched with JCPDS card number 01-073-1022. The crystal structure of MgV_3O_8 is monoclinic. The peaks in the diffraction pattern are indexed to (−202), (−221), (310), (−312), (−222), (022), (221), (−132), (−511), (−133), (042), (004), (133), (−315), (350), (260), (005), (−535), and (261) planes of MgV_3O_8 structure. There are three diffraction peaks corresponding to (111), (200), and (220) planes in doped XRD patterns, which indicate the presence of Ag species in the lattice (JCPDS # 00-004-0783) [29].

The average crystal size (D) is estimated by using the Debye-Scherrer's formula (equation (1))

$$D = \frac{k\lambda}{\beta \, Cos \, \theta} \tag{1}$$

Here D represents crystal size, k is shape constant (~0.94), λ is the wavelength of Cu kα = 1.54056 Å, β is full width at half maximum (FWHM), and θ is Bragg's angle. The average crystallite size estimated by using Scherrer's formula is given in Table 1, which shows the increase in the crystallite size with increasing the silver doping concentration. This is attributed to the difference between the ionic radii of substituting ions (Ag^+, 1.26 Å) with parent ions (Mg^{2+}, 0.72 Å). In brief, the XRD results exhibit that doping makes an increase in the crystallite size and transforms the crystal structure from orthorhombic to monoclinic for magnesium vanadate [30–32].

The lattice parameters for orthorhombic and monoclinic crystal structures are determined by using the following equations (2) and (3), respectively.

$$\frac{1}{d^2} = \frac{h^2}{a^2} + \frac{k^2}{b^2} + \frac{l^2}{c^2} \text{(Orthorhombic)} \tag{2}$$

$$\frac{1}{d^2} = \frac{1}{Sin^2 \, \beta}\left(\frac{h^2}{a^2} + \frac{k^2 \, Sin^2 \, \beta}{b^2} + \frac{l^2}{c^2} - \frac{2hlCos\beta}{ac}\right) \text{(Monoclinic)} \tag{3}$$

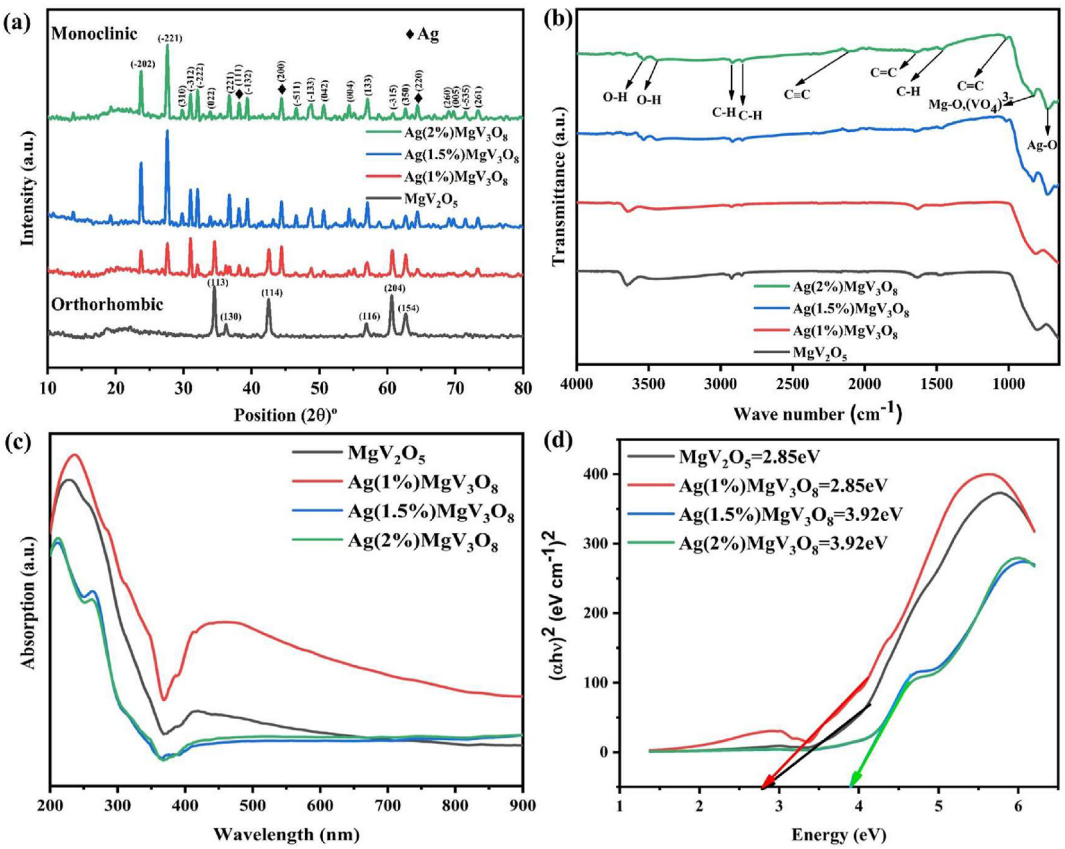

Fig. 2 – (a) X-ray diffraction patterns of magnesium vanadate and silver (different concentrations) doped magnesium vanadate nanomaterials, (b) FTIR spectra of undoped and silver-doped magnesium vanadate nanomaterials, (c) UV-Visible absorption curves, (d) Tauc's plot, of magnesium vanadate and silver doped magnesium vanadate.

Please cite this article as: Umair M et al., Predominated capacitive behavior of Ag-doped magnesium vanadate as a novel electrode material for supercapacitors, International Journal of Hydrogen Energy, https://doi.org/10.1016/j.ijhydene.2023.05.279

Table 1 – Crystallite size, lattice parameters, and volume of synthesized materials.

Sample	Crystallite size (nm)	Lattice parameters						Volume (Å^3)
		Experimental			Ref.			
		a (Å)	b (Å)	c (Å)	a (Å)	b (Å)	c (Å)	
MgV_2O_5	17	3.64	10.16	11.16	3.69	9.96	11.01	114.05
Ag (1%) MgV_3O_8	45	10.48	8.47	7.72	10.29	8.53	7.74	597.36
Ag (1.5%) MgV_3O_8	55	10.53	8.64	7.37	10.29	8.53	7.74	583.97
Ag (2%) MgV_3O_8	60	10	8.51	7.75	10.29	8.53	7.74	574.94

Where a,b, and c represent lattice parameters, h, k, and l are miller indices, d corresponds to inter atomic spacing, and the value of β is 119.5°. The unit cell volume is estimated by using the following equations (4) and (5);

$$V = abc(\text{Orthorhombic}) \quad (4)$$

$$V = (abc)\text{Sin}\ \beta(\text{Monoclinic}) \quad (5)$$

Functional groups of magnesium vanadate-based nanomaterials are further investigated by FTIR in the 650–4000 cm^{-1} range at room temperature (Fig. 2b). The transmittance band found in the range from 3443 to 3648 cm^{-1} is attributed to the OH stretching of water molecules. The bands detected in the range of 2848–2925 cm^{-1} belong to C–H stretching, whereas, bands at 1635, 1636, and 1652 cm^{-1} are related to the C=C stretching. The bands at wave numbers 1457, 1465, and 1488 cm^{-1} correspond to C–H bending. The new functional groups evolved at 2100, 1012 and 1017 cm^{-1} with silver doping which are assigned to the C≡C stretching and C=C bonding. The transmittance bands detected at 801, 812, and 828 cm^{-1} belong to VO_4^{-4}, VO_4^{-3}, and Mg–O, respectively [33]. The band located at 731 cm^{-1} clearly shows the presence of silver ions in the magnesium vanadate lattice as Ag–O bond [34–36].

The optical properties of magnesium vanadate and silver-doped magnesium vanadate are examined using UV-Visible spectroscopy. The absorption curves of MgV_2O_5 and Ag-doped MgV_3O_8 at different Ag concentrations (1%, 1.5%, 2%) are shown in Fig. 2c. The absorption spectrum of MgV_2O_5 shows a broad peak at 415 nm in the visible light region. Li et al. (2015) also reported the absorption spectra of different phases of magnesium vanadate to appear in the visible light region [37]. The increase in broadness and a red shift is clearly observed for silver (1%) doped magnesium vanadate. However, for 1.5% and 2.0% doped samples, the peak in the visible region is suppressed significantly, whereas, a new peak at 262 nm is appeared. The optical bandgap is determined by using well known Tauc's plot (equation (6)) [38];

$$\alpha h\nu = \beta\left(h\nu - E_g\right)^m \quad (6)$$

Here, β is a constant, α symbolize the absorption coefficient, h = Planck constant, ν stand for photon frequency, E_g denotes the energy band gap, and m factor represent the transition mode [39]. The direct band gap value of magnesium vanadate and Ag (1%) doped magnesium vanadate is ~2.85 eV. This band gap is in good accord with magnesium vanadate, which ranges from 2.2 eV to 3.1 eV [37] (Fig. 2d). However, further increase in silver doping increases the band gap to 3.92 eV. It is stated in the literature that Ag doping up to 3% can rise the optical band gap, whereas further increase in Ag concentration can narrow the band gap of the host material [40]. The Burstein Moss effect, which occurs due to a rise in carrier concentration, led the energy band gap to wider with doping concentration. Due to the constraints of solid dissolution at higher doping levels, electron density dropped, which slightly lowered conductivity [41].

The morphological analysis of synthesized magnesium vanadate and silver (2%) doped magnesium vanadate nanoparticles (NPs) is performed by SEM. The SEM images of MgV_2O_5 and Ag (2%) MgV_3O_8 are depicted in Fig. 3a and (c) respectively. SEM analysis shows that both the MgV_2O_5 and Ag (2%) MgV_3O_8 nanoparticles have spherical shape particles, however, Ag (2%) MgV_3O_8 also exhibits some large aggregates. Additionally, it is revealed that nanoparticles have smooth surface dense grains, demonstrating their excellent crystalline nature [42]. Fig. 3(b) and (d) display the size distribution histograms of the materials. The magnesium vanadate and silver doped magnesium vanadate have average particle sizes of 40 ± 10.5 nm and 55 ± 18.7 nm respectively, which clearly demonstrates that Ag^+ doping increases the particle size and is consistent with XRD results [43]. Additionally, EDX analysis is performed for compositional analysis of synthesized Ag (2%) MgV_3O_8 nanomaterials. EDX spectrum displays the peaks for silver (Ag), magnesium (Mg), vanadium (V), and oxygen (O) which affirms the purity of synthesized Ag (2%) MgV_3O_8 nanomaterials (Fig. 3e). The atomic percentages of Ag, Mg, V, and O are 1.89%, 19.36%, 17.44%, and 61.32% respectively. Silver doping is further verified by using EDX chemical mapping (Fig. 4a-f). The chemical maps show the distribution of respective elements in the Ag (2%) doped MgV_3O_8 material.

The bounding types and valence states of elements involved in Ag (2%) MgV_3O_8 composition are investigated by X-ray photoelectron spectroscopy (XPS). Fig. 5a demonstrates the survey spectrum of Ag (2%) MgV_3O_8, and depicts the features of Ag3d, Mg2s, V2p3, and O1s which further confirms the formation of the silver (2%) doped magnesium vanadate nanostructures. The high-resolution XPS spectrum for Ag3d shows doublet peaks which accommodate further four binding energies (Fig. 5b). The binding energies for Ag^0 $3d_{5/2}$ and Ag^0 $3d_{3/2}$ are detected at 365.4 and 374.4 eV respectively, whereas two higher peaks at 368 and 373 eV are allocated to Ag^+ $3d_{5/2}$ and Ag^+ $3d_{3/2}$ [23]. In the case of the Mg 2s spectrum, the binding energy peaks at 90.2 eV and 92 eV correspond to divalent Mg, while the peak at 88.66 eV is attributed to metallic Mg as shown in Fig. 5c [44–47]. The V 2p3 is divided into three sub-peaks (Fig. 5d). The broad peaks V $2p_{3/2}$ at binding energies of 516.4 eV and 515 eV correlate to V^{5+}cation, whereas the smaller peak at 510.4 is related to V^{4+}. According to these

Please cite this article as: Umair M et al., Predominated capacitive behavior of Ag-doped magnesium vanadate as a novel electrode material for supercapacitors, International Journal of Hydrogen Energy, https://doi.org/10.1016/j.ijhydene.2023.05.279

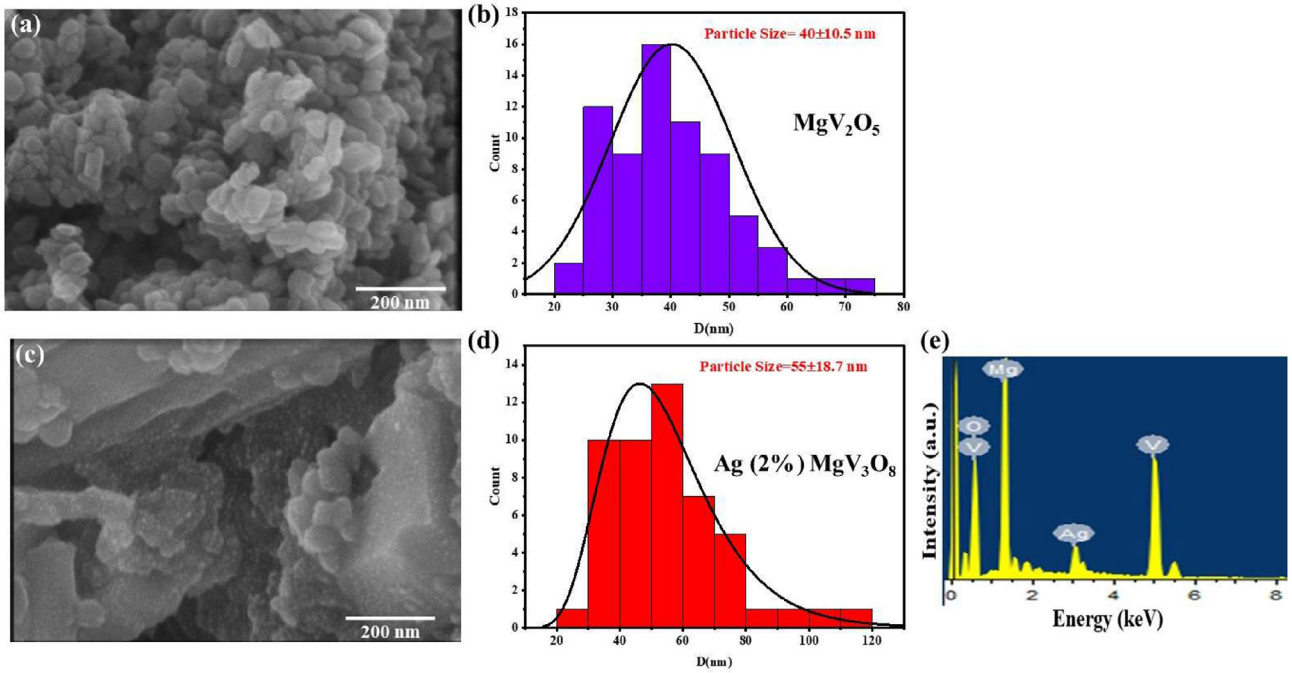

Fig. 3 – SEM micrographs and related size distributions of (a, b) Magnesium vanadate, (c, d) Ag (2%) doped magnesium vanadate, (e) EDX spectrum of Ag (2%) doped magnesium vanadate.

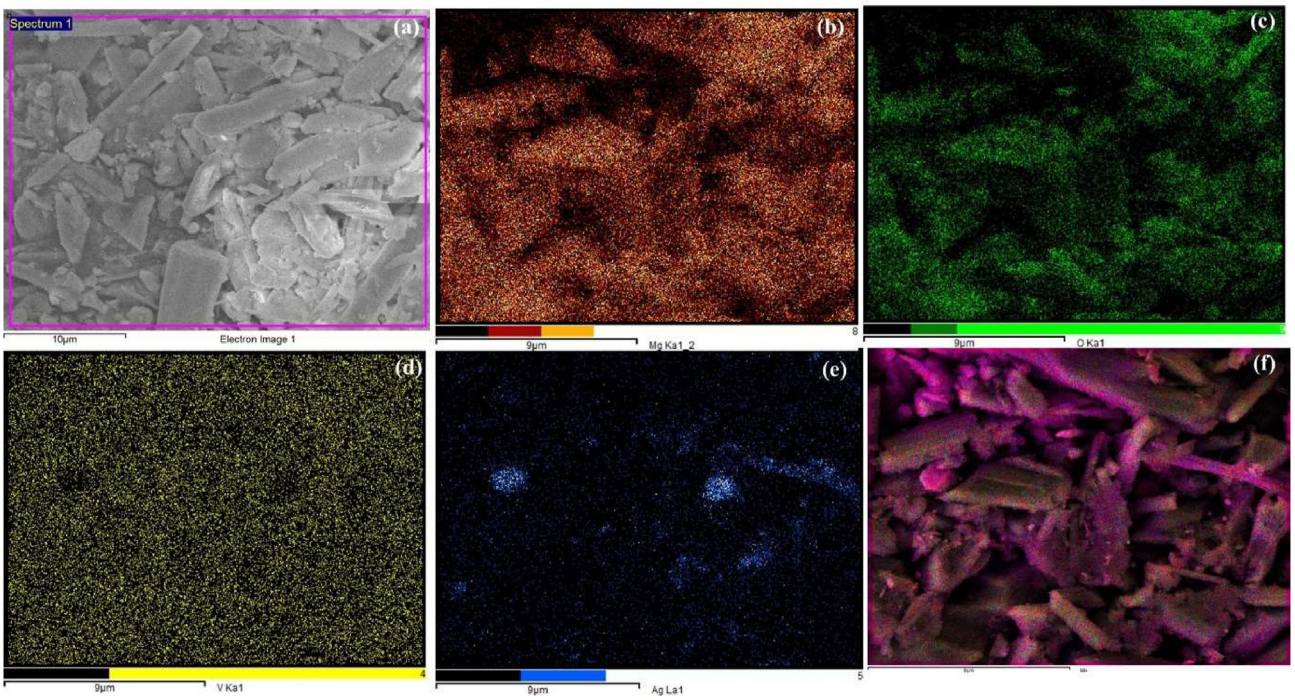

Fig. 4 – EDX chemical mapping of Ag (2%) doped MgV_3O_8 nanomaterials; (a) TEM image of selected area, chemical maps of (b) Mg, (c) O, (d) V, (e) Ag, (f) Overlay image of the chemical maps.

findings, V_3O_8 shows a mixed valence vanadium oxide nature [17,48,49] and can be useful for better electrochemical properties. In the case of the O 1s spectrum, three binding energy peaks are found. The peaks at 531.5 eV, 530 eV, and 525 eV are identified as lattice oxygen, O–V^{5+}, and O–V^{4+} respectively, and shown in Fig. 5e [49,50].

Electrochemical studies

Cyclic voltammetry investigates the capacitive behavior and the charge storage nature of materials. The CV measurements at different scan rates (5 mVs^{-1} to 60 mVs^{-1}) are performed to examine the electrochemical behavior of magnesium

Please cite this article as: Umair M et al., Predominated capacitive behavior of Ag-doped magnesium vanadate as a novel electrode material for supercapacitors, International Journal of Hydrogen Energy, https://doi.org/10.1016/j.ijhydene.2023.05.279

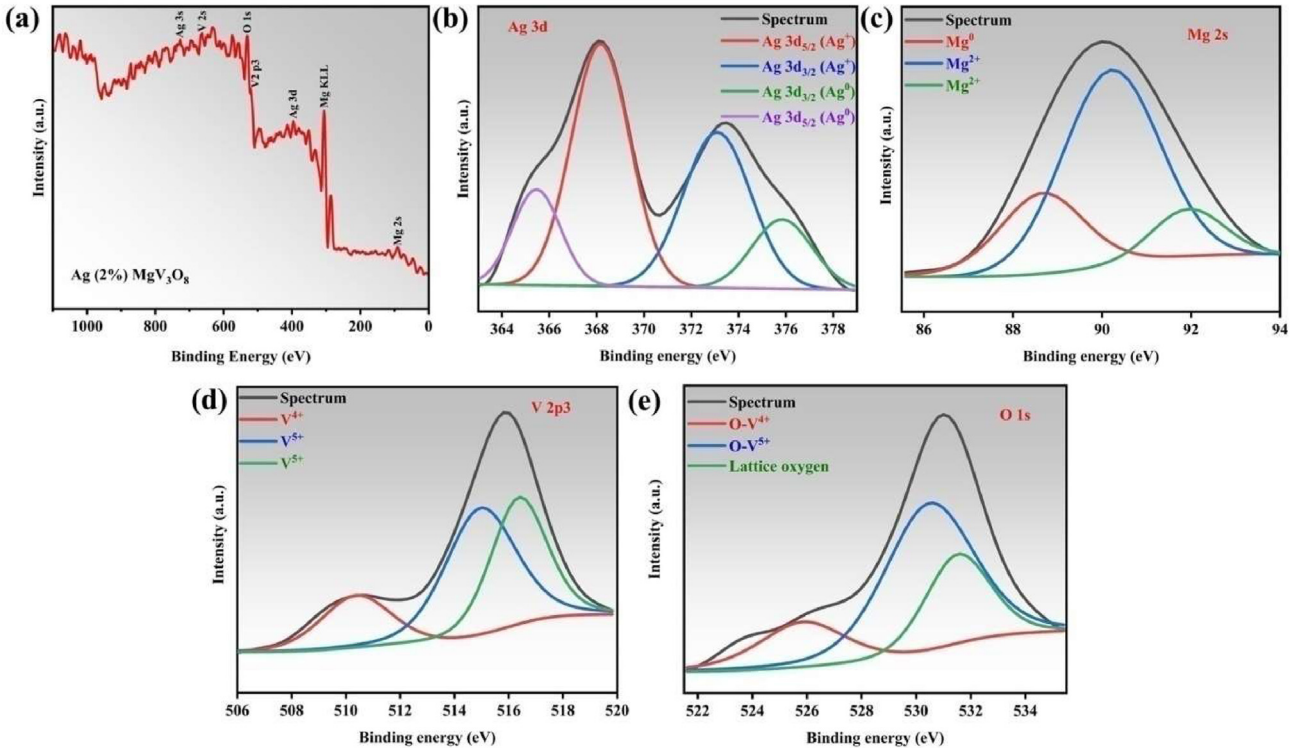

Fig. 5 – XPS analysis of Ag (2%) doped MgV_3O_8; (a) Survey spectrum. High-resolution spectra (b) Ag 3d, (c) Mg 2s, (d) V 2p3, (e) O 1s.

vanadate (MgV_2O_5) (Fig. 6a) and silver-doped magnesium vanadate [Ag (2%) MgV_3O_8] modified electrodes (Fig. 6b). All the CV spectra are determined in the potential window ranging from 0 to 0.6 V. The peaks appear in the anodic zone as a result of oxidation, whereas the peaks appear in the cathodic region as a result of the reduction reaction [51]. Fig. 6a shows CV profile changes with increasing the scan rates where single reduction peak changes to a doublet, however, the prominent peak still belongs to 0.31 V. Sometimes there are multiple peaks; this may indicate a cascade of electrochemical activities involving the same or distinct species that exist in the slurry at the surface of the electrode [52]. In the case of Ag (2%) MgV_3O_8, the reduction peak is more prominent, well defined (Fig. 6b) and positioned at 0.29 V. The Ag(2%)MgV_3O_8 modified electrode exhibits considerably larger CV area than the MgV_2O_5 modified electrode as shown in Fig. 6c, which confirms the enhanced specific capacitance of the Ag(2%)MgV_3O_8 [53]. This improved response makes Ag (2%) MgV_3O_8 nanoparticles noble for electrode material in supercapacitor applications. Pseudo-capacitive nature is further revealed by the non-rectangular shape of CV in undoped and doped samples. The possible redox mechanism is given below

$$MgV_2O_5 + KOH \rightarrow MgOH + V_2O_5 + K^{+1} + e^{-1} \quad (7)$$

$$Ag^{+} + e^{-} \rightleftharpoons Ag \quad (8)$$

$$MgV_3O_8 + KOH \rightarrow MgOH + V_3O_8 + K^{+1} + e^{-1} \quad (9)$$

The specific capacitance (C_s) is estimated by using the relation (10) [54].

$$C_s = \frac{\int I \times \Delta V}{m \times \Delta V \times \nu} \quad (10)$$

Where $\int I \times \Delta V$ = area enclosed by the CV curve, ν = scan rate, m symbolizes the mass of active material, and ΔV = potential window. The estimated value of specific capacitance for MgV_2O_5 is~ 704 Fg^{-1}, 676 Fg^{-1}, 620 Fg^{-1}, 587 Fg^{-1}, 565 Fg^{-1}, 546 Fg^{-1}, and 535 Fg^{-1} at the scan rate 5 mVs^{-1}, 10 mVs^{-1}, 20 mVs^{-1}, 30 mVs^{-1}, 40 mVs^{-1}, 50 mVs^{-1}, and 60 mVs^{-1}, respectively. The specific capacitance increases to 920 Fg^{-1}, 757 Fg^{-1}, 666 Fg^{-1}, 634 Fg^{-1}, 616 Fg^{-1}, 606 Fg^{-1}, 596 Fg^{-1} for Ag (2%) MgV_3O_8 at the same scan rates. The specific capacitance drops as the scan rate increases due to a rise in resistance (Fig. 6d) [55]. The incorporation of Ag to the magnesium vanadate improved its conductivity and specific capacitance rises from 704 Fg^{-1} to 920 Fg^{-1} at scan rate of 5 mVs^{-1} because silver atoms engage in redox processes that provide a pseudo-capacitance contribution to Ag (2%) MgV_3O_8 [56].

The Randles-Sevick plot is used for the estimation of current contributions due to diffusive-controlled (faradaic) and surface-controlled (non-faradic) processes [57]. Fig. 7a,b shows the linearly fitted Randles plot for anodic and cathodic peaks. In each case, the main graph indicates the material's non-faradic behavior, while the inset shows the faradaic response. The correlation coefficient (R^2) values indicate the absolute mechanism of charge storage. The value of R^2 is

Please cite this article as: Umair M et al., Predominated capacitive behavior of Ag-doped magnesium vanadate as a novel electrode material for supercapacitors, International Journal of Hydrogen Energy, https://doi.org/10.1016/j.ijhydene.2023.05.279

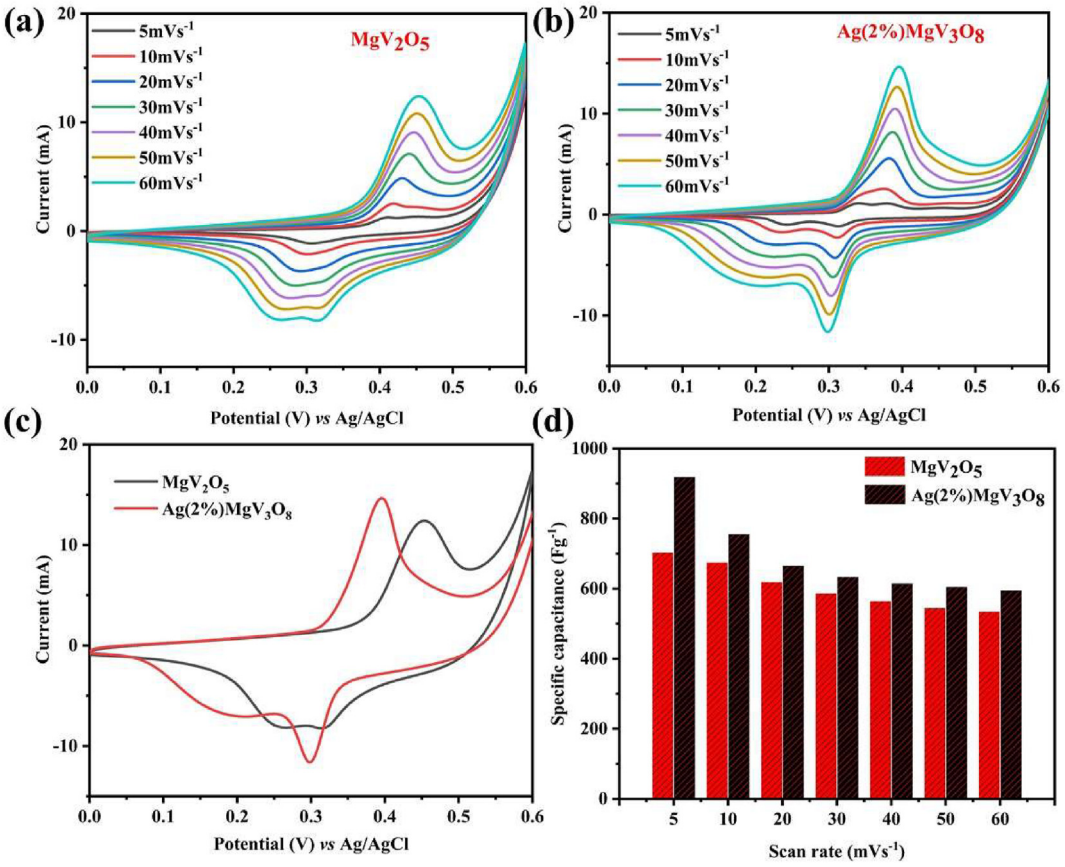

Fig. 6 – (a) CV curves of MgV_2O_5, (b)Ag (2%) MgV_3O_8 at scan rates from 5 mV/s to 60 mV/s, (c) Comparative CV curves of MgV_2O_5 and Ag (2%) MgV_3O_8 at 60 mV/s scan rate, (d) Specific capacitance variation with scan rate of MgV_2O_5 and Ag (2%) MgV_3O_8 based electrodes.

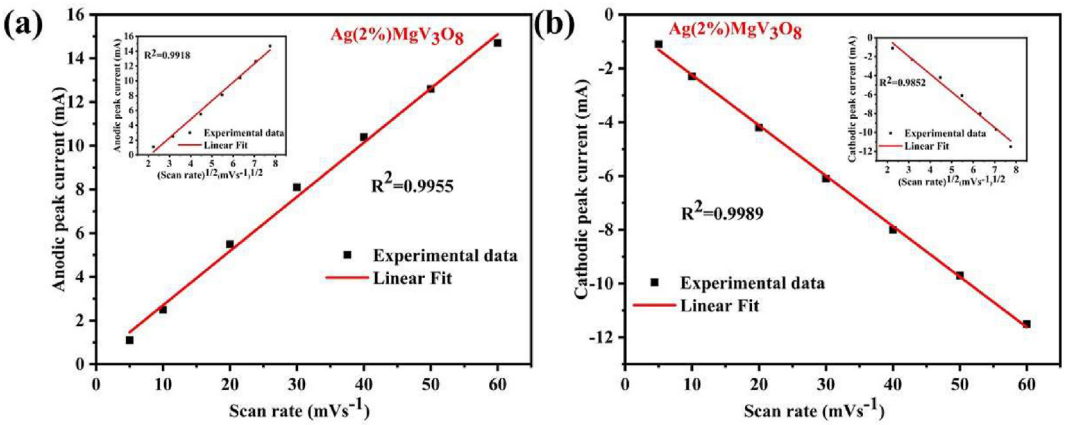

Fig. 7 – Faradaic/non-faradic contribution in Ag (2%) MgV_3O_8: (a) Anodic peaks, (b) Cathodic peaks.

0.9918 and 0.9955 for faradaic and non-faradic graphs, respectively which indicates that both processes contributed equally to the electrochemical response (Fig. 7a). The cathodic peaks show identical behavior as presented in the case of anodic peaks and provide evidence of the high reversibility and permanence nature of the material (Fig. 7b).

The electro-kinetics of the charge storage mechanism are understood by examining CV curves at different scan rates. A relatively quick surface-controlled process and a slower diffusion-controlled mechanism determine the charge storage in the electrode [58]. Dunn's model offers a novel method for investigating various charge storage mechanisms. The CV data at different scan rates are carefully examined to define capacitive effects by using the power's law (equation (11))

$$Ip = a\,\nu^{b} \tag{11}$$

Please cite this article as: Umair M et al., Predominated capacitive behavior of Ag-doped magnesium vanadate as a novel electrode material for supercapacitors, International Journal of Hydrogen Energy, https://doi.org/10.1016/j.ijhydene.2023.05.279

The equation can be modified further to equation (12) and equation 13

$$\log(Ip) = \log(a) + b\log(\nu) \quad (12)$$

$$\frac{\log(Ip)}{\log(\nu)} = b + \log(a) \quad (13)$$

here, Ip symbolizes the redox peak current, ν = scan rate, and both a and b are constant. There are two distinct conditions, the first is b = 0.5 and the second is b = 1. When b = 0.5, the diffusion-controlled process occurred, while, b = 1 represents the surface-controlled process. The linear fit provides the value of b = 1, which suggests surface controlled process or predominantly capacitive nature of the material (Fig. 8a) [59,60].

The value of b is also determined at different fixed potentials ranges from 0.25 V to 0.52 V (Fig. 8b). At the lowest potential of 0.25 V, the b value is 0.87 which decreases when the peak potential increases. The lowest b value is 0.55 at potential 0.34 V then rises again with the increases in potential (Fig. 8c). This fluctuation reveals that current emanates from the surface-controlled process which gradually transforms into diffusion-controlled process with an increase in potential. The maximum current at peak potentials is ascribed to a surface-controlled mechanism which is in good accord with the reported work of Wang et al. (2007) [60].

We can also quantify the capacitive contribution to the current behavior by paying closer attention to the CV scan rate dependency. The total current contribution at fixed potential is expressed by combining two distinct currents i.e. capacitive and diffusive mechanisms. equation (14) is given below [61].

$$I(V) = I_c + I_d \quad (14)$$

According to the Randles-Sevick equation, ($I_c \propto \nu$) and ($I_d \propto \sqrt{\nu}$) Therefore, the above equation can transform into equation 15

$$I(V) = K_1\nu + K_2\sqrt{\nu} \quad (15)$$

here, the $K_1\nu$ and $K_2\sqrt{\nu}$ belong to the capacitive and diffusion-limited contributions respectively.

This can be adjusted to equation 16

$$I(V) / \sqrt{\nu} = K_1\sqrt{\nu} + K_2 \quad (16)$$

The K_1 and K_2 values are determined by using Fig. 9a at different fixed potentials. By figuring out K_1 and K_2, we can quantify the percentage of each current contribution. Fig. 9b shows that when the scan rate increases, capacitive current surpasses diffusive current. It is depicted that at a scan rate of 60 mVs^{-1}, Ag (2%) MgV_3O_8 displays a very high capacitive contribution of 90.90%. These outcomes show that pseudo-

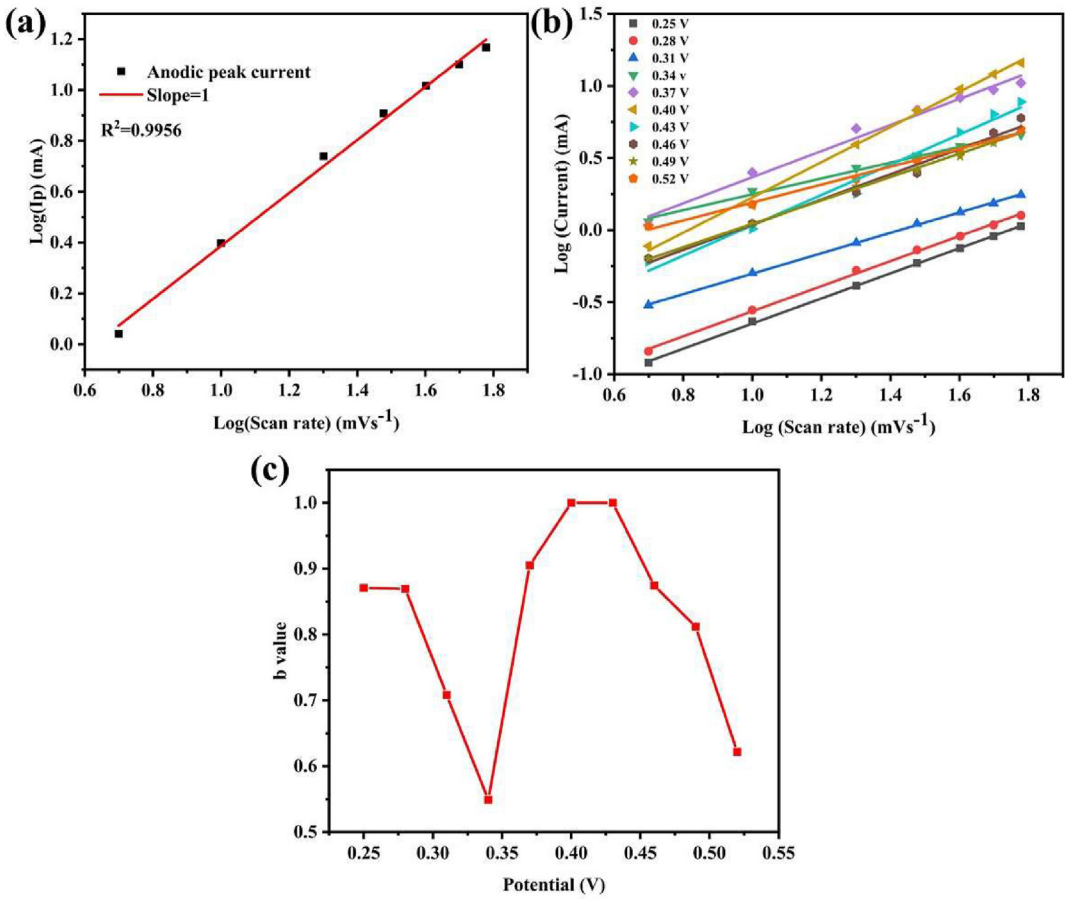

Fig. 8 – Charge storage mechanism in Ag (2%) MgV_3O_8 (a) Plot between log (anodic peak current) and log (scan rate) to determine b, (b) Plot between log (current) and log (scan rate) at different fixed potentials, (c) Variation in b at different fixed potentials.

Please cite this article as: Umair M et al., Predominated capacitive behavior of Ag-doped magnesium vanadate as a novel electrode material for supercapacitors, International Journal of Hydrogen Energy, https://doi.org/10.1016/j.ijhydene.2023.05.279

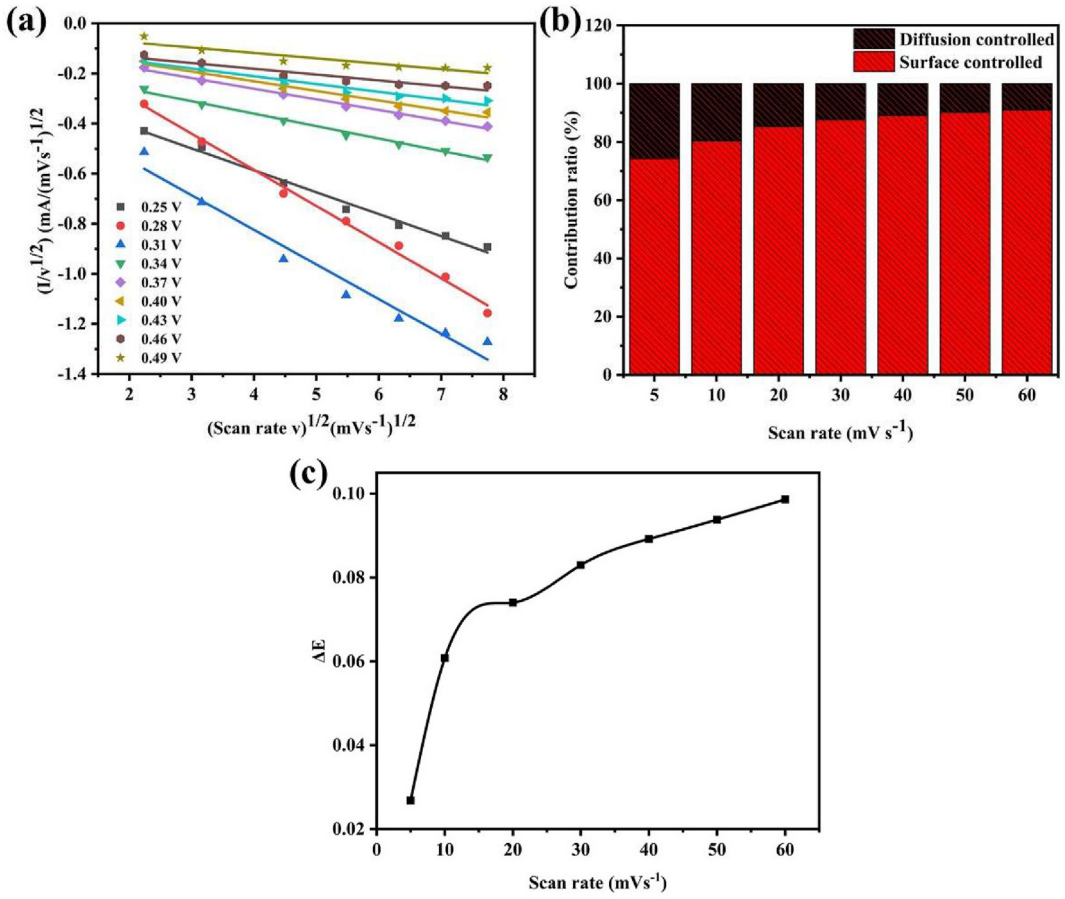

Fig. 9 – (a) Plot for k_1 and k_2 determination, (b) current contributions at different scan rates, (c) graph between (ΔE) of redox peaks and scan rates.

capacitive-dominated behavior is favorable for providing a fast charging and discharging rate [62–64]. When the scan rate increases, the change in potential (ΔE) between redox peaks rises. This is shown in Fig. 9c and may be attributed to the polarization effects.

The galvanostatic charge-discharge (GCD) technique is also used to evaluate the electrochemical performance of fabricated electrodes. GCD curves of MgV_2O_5 and Ag (2%) MgV_3O_8 modified electrodes are obtained at different current densities (5, 10, 15, and 25 Ag^{-1}) are shown in Fig. 10 (a, b). The GCD curves have non-linear behavior. It is depicted that the silver (2%) doped magnesium vanadate has a longer discharging time than magnesium vanadate, might be related to the fact that it has higher electrical conductivity [55]. The specific capacitance is also calculated using GCD curves (Equation (17)).

$$C_s = \frac{I \times \Delta t}{m \times \Delta V} \tag{17}$$

Here, I belong to applied current density, m = mass of active material, Δt and ΔV correspond to discharge time and potential difference respectively. The specific capacitance for MgV_2O_5 is 325 Fg^{-1}, 315 Fg^{-1}, 254 Fg^{-1}, and 117 Fg^{-1} at the current density 5 Ag^{-1}, 10 Ag^{-1}, 15 Ag^{-1}, and 25 Ag^{-1} respectively, whereas, in the case of Ag (2%) MgV_3O_8, the specific capacitance is determined as 706 Fg^{-1}, 666 Fg^{-1}, 592 Fg^{-1}, and 364 Fg^{-1} at the same current densities. The specific capacitance drops when the current density rises (Fig. 10c). For example, the specific capacitance drops from 706 Fg^{-1} to 364 Fg^{-1} when the current density increases from 5 Ag^{-1} to 25 Ag^{-1}. The drop in specific capacitance value may be due to the electrolyte ion's slow interaction with the surface of the electrode at higher applied current densities and their slow diffusion across the electrolyte/electrode interface [65]. The Ag (2%) MgV_3O_8 has much superior electrochemical performance over the MgV_2O_5 electrode consistent with CV results because silver exhibits higher conductivity, mechanical rigidity, and significant surface area which leads to highest specific capacitance. Zhao et al. (2017) reported that Ag network may also significantly improve the mechanical strength of the electrode [66]. The comparison with other previously reported materials is also provided in Table 2. The coulombic efficiency of 87% is observed after 3000 cycles for Ag (2%) MgV_3O_8 as shown in Fig. 10d.

The energy density (E_d) and power density (P_d) are also determined from the GCD curve by using equations (18) and (19) respectively [53,55,71].

$$E_d = \frac{1}{2} C_s (\Delta V)^2 \tag{18}$$

$$P_d = \frac{E_d}{\Delta t} \tag{19}$$

Please cite this article as: Umair M et al., Predominated capacitive behavior of Ag-doped magnesium vanadate as a novel electrode material for supercapacitors, International Journal of Hydrogen Energy, https://doi.org/10.1016/j.ijhydene.2023.05.279

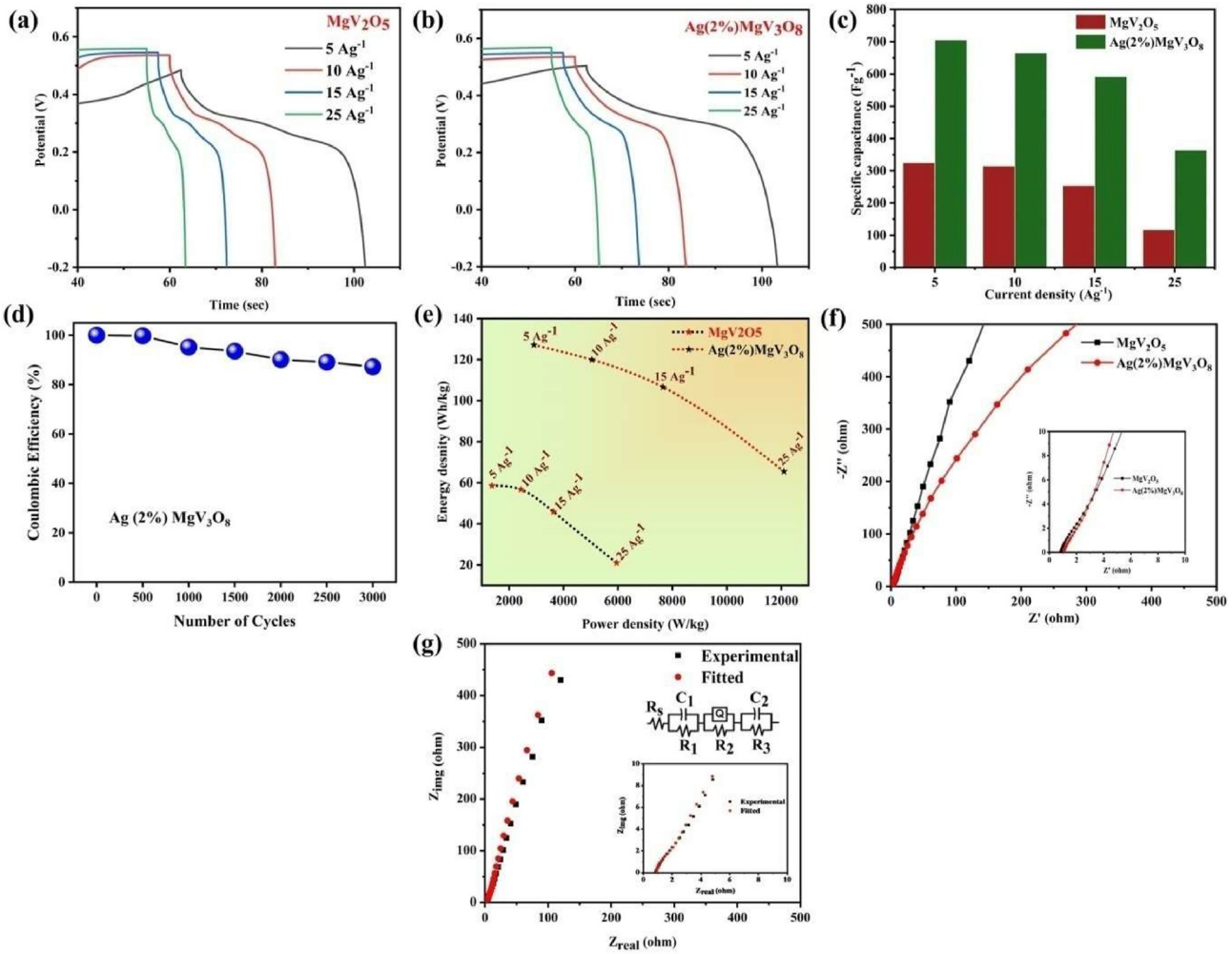

Fig. 10 – GCD curves; (a) MgV_2O_5, (b) Silver (2%) doped magnesium vanadateat 5, 10, 15, 25 Ag^{-1} current densities, (c) Specific capacitance of MgV_2O_5 and Ag (2%) MgV_3O_8 at different current densities, (d) Coulombic efficiency of Ag (2%) MgV_3O_8 based electrode for 3000 cycles, (e) Energy density and power density variations, (f) The Nyquist plots comparison of magnesium vanadate and silver (2%) doped magnesium vanadate (inset: high frequency spectra), (g) Fitting for equivalent series model (inset: equivalent circuit).

Table 2 – Comparison of reported specific capacitance of magnesium vanadate and silver-based electrode materials.

Electrode material	Current density	Specific capacitance	Ref.
MgV_2O_5-NC composite	2 Ag^{-1}	358 Fg^{-1}	[21]
Mn_3O_4	0.5 Ag^{-1}	302 Fg^{-1}	[67]
Cr-doped Mn_3O_4	0.5 Ag^{-1}	272 Fg^{-1}	[68]
MnV_2O_6	0.5 Ag^{-1}	348 Fg^{-1}	[69]
$AgVO_3$	1 Ag^{-1}	243 mA hg^{-1}	[23]
$Ag_4V_2O_7$	1 Ag^{-1}	548 Cg^{-1}	[70]
$Ag/AgVO_3$	50 mA g^{-1}	242 mA hg^{-1}	[24]
MgV_2O_5	5 Ag^{-1}	325 Fg^{-1}	Present work
Ag (2%) MgV_3O_8	5 Ag^{-1}	706 Fg^{-1}	Present work

where C_s denotes the specific capacitance, ΔV symbolizes the potential window, and Δt represents discharging time. The doped magnesium vanadate modified electrode exhibit a higher power density of 12,100 Wkg^{-1} with an energy density of 65.5 $Whkg^{-1}$ at 25 Ag^{-1} current density. Fig. 10e displays the calculated (E_d) and (P_d) for Ag (2%) MgV_3O_8 and MgV_2O_5 modified electrodes.

Electrochemical impedance spectroscopy (EIS) is used to determine electron transfer behavior of the prepared electrodes [72]. EIS analyzed the electron transfer process and conductivity parameters of fabricated magnesium vanadate and silver (2%) doped magnesium vanadate electrodes. There are two methods for presenting impedance data one is the Bode plot and the other is the Nyquist plot. The Nyquist plot draws between imaginary and real impedances. Impedance data is commonly captured and presented from high-frequency to low-frequency domains [73]. The Nyquist plot having EIS spectra of both materials is shown in Fig. 10f. The charge transfer of electrons in both electrodes (doped and undoped) is monitored by using charge transfer resistance (R_{CT}). The R_{CT} value for magnesium vanadate and silver (2%) doped magnesium vanadate modified electrodes at high-frequency region have been determined as 5.9 Ω and 5 Ω respectively. It is depicted that doped material has a smaller

Please cite this article as: Umair M et al., Predominated capacitive behavior of Ag-doped magnesium vanadate as a novel electrode material for supercapacitors, International Journal of Hydrogen Energy, https://doi.org/10.1016/j.ijhydene.2023.05.279

value of R_{ct} than undoped. The transport of ions into electroactive material can be assisted by the lower resistance [74]. The conclusions support the theory that a silver (2%) doped magnesium vanadate modified electrode is more effective in process of transferring electrons. The EIS study of silver (2%) doped magnesium vanadate is evaluated by fitting equivalent circuit analysis (R(CR)(QR)(CR)) as shown in Fig. 10g. A series of components are used to construct the model where R_s affirmed the solution resistance of the prepared electrode and KOH electrolyte. R_1 is the charge transfer resistance and C_1 corresponds to capacitance. Q indicates the constant phase element which is connected side by side with R_2 (resistance) to provide the series connection to R_1, C_2, and R_3 correspond to capacitor and resistance respectively [75–77].

Conclusion

Silver-doped magnesium vanadate nanomaterials (1%, 1.5%, 2%) are successfully prepared by using a simple hydrothermal process. When utilized as electrodes for supercapacitor, MgV_2O_5 and Ag (2%) MgV_3O_8 nanomaterials revealed the remarkable pseudo capacitance effect. The MgV_2O_5-based electrode materials display the specific capacitance of 325 Fg^{-1} at a current density of 5 Ag^{-1}. The capability to store electrochemical energy is improved considerably by doping of silver. Thus, the electrochemical performance of Ag (2%) MgV_3O_8 electrodes attained their highest specific capacitance of 706 Fg^{-1} at a current density of 5 Ag^{-1}. Further, the fabricated silver-modified electrode exhibits low resistance, with a maximum energy density of 65.5 $Whkg^{-1}$ and power density of 12,100 Wkg^{-1}, which can perform as an excellent energy storage source. Our study opens up new avenues for developing an electrode for high-performance energy storage purposes such as supercapacitors in the future.

Declaration of competing interest

The authors declare that they have no known competing financial interests or personal relationships that could have appeared to influence the work reported in this paper.

Acknowledgments

The authors would like to acknowledge the financial assistance from the Higher Education Commission (HEC) of Pakistan, for providing funds under NRPU Research Project No: 7487/Punjab/NRPU/R&D/HEC/2017.

REFERENCES

[1] Banerjee J, Dutta K. An overview on the use of metal vanadium oxides and vanadates in supercapacitors and rechargeable batteries. Int J Energy Res 2022;46(4):3983–4000.
[2] Zhu S, et al. CdTe and Ag nanoparticles co-modified TiO2 nanotube arrays for the enhanced wastewater treatment and hydrogen production. J Environ Chem Eng 2022;10(2):107207.
[3] Wang S, et al. Synergetic function of the single-atom Ru–N4 site and Ru nanoparticles for hydrogen production in a wide pH range and seawater electrolysis. ACS Appl Mater Interfaces 2022;14(13):15250–8.
[4] EzhilArasi S, et al. Enhanced electrochemical performance of copper vanadate nanorods as an electrode material for pseudocapacitor application. J Mater Sci Mater Electron 2020;31(9):7012–21.
[5] Maroušek J. Nanoparticles can change (bio) hydrogen competitiveness. Fuel 2022;328:125318.
[6] Zhang J, et al. Photocatalytic hydrogen production from seawater under full solar spectrum without sacrificial reagents using TiO2 nanoparticles. Nano Res 2022;15(3):2013–22.
[7] Aygun A, et al. Highly active PdPt bimetallic nanoparticles synthesized by one-step bioreduction method: characterizations, anticancer, antibacterial activities and evaluation of their catalytic effect for hydrogen generation. Int J Hydrogen Energy 2023;48(17):6666–79.
[8] Liao J, et al. Interfacial charge transfer induced dual-active-sites of heterostructured Cu0. 8Ni0. 2WO4 nanoparticles in ammonia borane methanolysis for fast hydrogen production. Appl Catal B Environ 2023;320:121973.
[9] Qiu P, et al. Co-implantation of oxygen vacancy and well-dispersed Cu cocatalyst into TiO2 nanoparticles for promoting solar-to-hydrogen evolution. Int J Hydrogen Energy 2023;48(3):933–42.
[10] Yao G, et al. Nanostructured transition metal vanadates as electrodes for pseudo-supercapacitors: a review. J Nanoparticle Res 2021;23(2):1–27.
[11] Chen GZ. Supercapacitor and supercapattery as emerging electrochemical energy stores. Int Mater Rev 2017;62(4):173–202.
[12] Kumar R, et al. An overview of recent progress in nanostructured carbon-based supercapacitor electrodes: from zero to bi-dimensional materials. Carbon 2022;193:298–338.
[13] Yan Y, et al. Vanadium based materials as electrode materials for high performance supercapacitors. J Power Sources 2016;329:148–69.
[14] Li X, et al. High-performance surface optimized Mg-doped V2O5 (Mg@ V2O5) cathode material via a surfactant-assisted hydrothermal technology for lithium-ion and lithium-sulfur batteries. Ionics 2022;28(4):1511–21.
[15] Deng W, et al. High-capacity layered magnesium vanadate with concentrated gel electrolyte toward high-performance and wide-temperature zinc-ion battery. ACS Nano 2020;14(11):15776–85.
[16] Lee J, et al. Synthesis and characterization of magnesium vanadates as potential magnesium-ion cathode materials through an ab initio guided carbothermal reduction approach. Angew Chem 2022;134(8):e202112688.
[17] Xiao F, et al. Embedding of Mg-doped V 2 O 5 nanoparticles in a carbon matrix to improve their electrochemical properties for high-energy rechargeable lithium batteries. J Mater Chem 2017;5(33):17432–41.
[18] Xu X, et al. Alkaline earth metal vanadates as sodium-ion battery anodes. Nat Commun 2017;8(1):1–11.
[19] Zhou W, et al. An environmentally adaptive quasi-solid-state zinc-ion battery based on magnesium vanadate hydrate with commercial-level mass loading and anti-freezing gel electrolyte. J Mater Chem 2020;8(17):8397–409.
[20] Xu X, et al. Vanadium-based nanomaterials: a promising family for emerging metal-ion batteries. Adv Funct Mater 2020;30(10):1904398.
[21] Santhoshkumar P, et al. One-pot hydrothermal synthesis of MgV2O5-NC porous composite for hybrid supercapacitors

Please cite this article as: Umair M et al., Predominated capacitive behavior of Ag-doped magnesium vanadate as a novel electrode material for supercapacitors, International Journal of Hydrogen Energy, https://doi.org/10.1016/j.ijhydene.2023.05.279

with enhanced storage properties. J Alloys Compd 2022;908:164598.
[22] Siva Vijayakumar T, et al. Synthesis of silver-doped zinc oxide nanocomposite by pulse mode ultrasonication and its characterization studies. J Nanosci 2013;2013:1–7.
[23] Li H, et al. Facile synthesis, characterization, and electrochemical performance of multi-scale AgVO3 particles. J Alloys Compd 2016;674:56–62.
[24] Liang S, et al. Facile synthesis of Ag/AgVO3 hybrid nanorods with enhanced electrochemical performance as cathode material for lithium batteries. J Power Sources 2013;228:178–84.
[25] Heydari H, Gholivand MB. A novel high-performance supercapacitor based on high-quality CeO 2/nitrogen-doped reduced graphene oxide nanocomposite. Appl Phys A 2017;123:1–10.
[26] Iqbal MZ, et al. Strategies to enhance the electrochemical performance of strontium-based electrode materials for battery-supercapacitor applications. J Electroanal Chem 2022;924:116868.
[27] Iqbal MZ, et al. Cobalt intercalated redox active 1, 2, 4, 5-benzene-tetra-carboxylic acid-pyridine-3, 5-dicarboxylic acid bi-linker organic framework for state-of-the-art battery-supercapacitor hybrids. Mater Today Sustaina 2023;21:100286.
[28] Zhao H, et al. Vanadium oxides–reduced graphene oxide composite for lithium-ion batteries and supercapacitors with improved electrochemical performance. J Power Sources 2013;222:21–31.
[29] Xu X, et al. New insights into Ag-doped BiVO 4 microspheres as visible light photocatalysts. RSC Adv 2016;6(101):98788–96.
[30] Kumar KS, et al. Physical properties of spray pyrolyzed Ag-doped SnS thin films for opto-electronic applications. Mater Lett 2014;131:167–70.
[31] Modaresi N, et al. Competition between the impact of cation distribution and crystallite size on properties of MnxFe3−xO4 nanoparticles synthesized at room temperature. Ceram Int 2017;43(17):15381–91.
[32] Sarica E, Bilgin V. Study of some physical properties of ultrasonically spray deposited silver doped lead sulphide thin films. Mater Sci Semicond Process 2017;68:288–94.
[33] Celik G, Somunkiranoglu S, Kurtulus F. Hydrothermal synthesis and characterization of double phase magnesium vanadium oxides. Manuf Eng 2014;63(2):53–7.
[34] Fadhil ES, Ahmed L, Mohammed AF. Effect of silver doping on structural and photocatalytic circumstances of ZnO nanoparticles. Iraqi J Nanotechnol 2020;(1):13–22.
[35] Sampurnam S, et al. Synthesis, characterization, and photocatalytic activity of silver nanoparticledoped phosphomolybdic acid supportedZirconia. Mater Today Proc 2019;14:558–62.
[36] Siva Vijayakumar T, et al. Synthesis of silver-doped zinc oxide nanocomposite by pulse mode ultrasonication and its characterization studies. Journal of Nanosci 2013;2013.
[37] Li P, et al. Effects of cation concentration on photocatalytic performance over magnesium vanadates. Apl Mater 2015;3(10):104405.
[38] Weckhuysen BM. Ultraviolet-visible spectroscopy. 2004.
[39] Makuła P, Pacia M, Macyk W. How to correctly determine the band gap energy of modified semiconductor photocatalysts based on UV-Vis spectra. ACS Publications; 2018. p. 6814–7.
[40] Singh P, et al. Optical band gap tuning of Ag doped Ge2Sb2Te5 thin films. J Mater Sci Mater Electron 2017;28(15):11300–5.
[41] Narayanan N, Nk D. Ga dopant induced band gap broadening and conductivity enhancement in spray pyrolysed Zn 0.85 Ca 0.15 O thin films. Mater Res 2018:21.
[42] Faheem M, et al. Rapid single-step synthesis and crystal structure analysis of Cu: ZnO photocatalyst for efficient degradation of reactive dyes under UV-visible light irradiation. Arabian J Sci Eng 2022:1–17.
[43] Chauhan V, et al. Greenish-yellow emission from rare-earth free Li+ doped zinc vanadate phosphor. Results Phys 2022:105689.
[44] Ahmad A, et al. Bio-construction of MgO nanoparticles using Texas sage plant extract for catalytical degradation of methylene blue via photocatalysis. Int J Environ Sci Technol 2022:1–12.
[45] Strohmeier BR. Magnesium aluminate (MgAl2O4) by XPS. Surf Sci Spectra 1994;3(2):121–7.
[46] Talapatra A, et al. X-ray photoelectron spectroscopy studies of MgB2 for valence state of Mg. Physica C: Supercond 2005;419(3–4):141–7.
[47] Le Febvrier A, Jensen J, Eklund P. Wet-cleaning of MgO (001): modification of surface chemistry and effects on thin film growth investigated by x-ray photoelectron spectroscopy and time-of-flight secondary ion mass spectroscopy. J Vac Sci Technol A 2017;35(2):021407.
[48] Lai K, et al. Preparation and characterization of novel alkylviologens-intercalated vanadyl-vanadate (RV) V3O8. J Solid State Chem 2011;184(9):2393–7.
[49] Liu P, et al. Ultrathin nanoribbons of in situ carbon-coated V3O7· H2O for high-energy and long-life Li-ion batteries: synthesis, electrochemical performance, and charge–discharge behavior. ACS Appl Mater Interfaces 2017;9(20):17002–12.
[50] Khawar MR, et al. Cerium oxide nanosheets-based tertiary composites (CeO2/ZnO/ZnWO4) for supercapattery application and evaluation of faradic & non-faradic capacitive distribution by using Donn's model. J Energy Storage 2022;55:105778.
[51] Arasi SE, et al. Studies on electrochemical mechanism of nanostructured cobalt vanadate electrode material for pseudocapacitors. J Energy Storage 2021;41:102986.
[52] Elgrishi N, et al. A practical beginner's guide to cyclic voltammetry. J Chem Educ 2018;95(2):197–206.
[53] Qu Z, et al. An efficient binder-free electrode with multiple carbonized channels wrapped by NiCo2O4 nanosheets for high-performance capacitive energy storage. J Power Sources 2019;410:179–87.
[54] Alqarni AN, et al. Synthesis and design of vanadium intercalated spinal ferrite (Co0. 5Ni0. 5VxFe1. 6− xO4) electrodes for high current supercapacitor applications. J Energy Storage 2022;51:104357.
[55] Asghar A, et al. Enhanced electrochemical performance of hydrothermally synthesized NiS/ZnS composites as an electrode for super-capacitors. J Cluster Sci 2022;33(5):2325–35.
[56] Wasfey MA, et al. Nickel cobaltite functionalized silver doped carbon xerogels as efficient electrode materials for high performance symmetric supercapacitor. Materials 2020;13(21):4906.
[57] Mathis TS, et al. Energy storage data reporting in perspective—guidelines for interpreting the performance of electrochemical energy storage systems. Adv Energy Mater 2019;9(39):1902007.
[58] Guo F, Gupta N, Teng X. Enhancing pseudocapacitive process for energy storage devices: analyzing the charge transport using electro-kinetic study and numerical modeling, vol. 87. Supercapacitors: Theoretical and Practical Solutions; 2018.
[59] Kurra N, et al. Bistacked titanium carbide (MXene) anodes for hybrid sodium-ion capacitors. ACS Energy Lett 2018;3(9):2094–100.

Please cite this article as: Umair M et al., Predominated capacitive behavior of Ag-doped magnesium vanadate as a novel electrode material for supercapacitors, International Journal of Hydrogen Energy, https://doi.org/10.1016/j.ijhydene.2023.05.279

[60] Wang J, et al. Pseudocapacitive contributions to electrochemical energy storage in TiO2 (anatase) nanoparticles. J Phys Chem C 2007;111(40):14925–31.
[61] Huang H. Pseudocapacitive materials for high-power Li+/Na+ storage. ETH Zurich; 2019.
[62] Huang H, et al. Layered metal vanadates with different interlayer cations for high-rate Na-ion storage. J Mater Chem 2019;7(27):16109–16.
[63] Joshi A, Saini S, Chand P. Electrochemical behaviour of temperature-based bismuth phosphate nanostructures for energy storage application. Chem Phys Lett 2022;804:139898.
[64] Wei Q, et al. High-energy and high-power pseudocapacitor–battery hybrid sodium-ion capacitor with Na+ intercalation pseudocapacitance anode. Nano-Micro Lett 2021;13(1):1–13.
[65] Elgendy A, et al. Mesoporous Ni-Zn-Fe layered double hydroxide as an efficient binder-free electrode active material for high-performance supercapacitors. J Power Sources 2020;466:228294.
[66] Zhao Q, et al. One dimensional silver-based nanomaterials: preparations and electrochemical applications. Small 2017;13(38):1701091.
[67] Qiao Y, et al. A modified solvothermal synthesis of porous Mn3O4 for supercapacitor with excellent rate capability and long cycle life. J Alloys Compd 2016;660:416–22.
[68] Dong R, et al. Enhanced supercapacitor performance of Mn3O4 nanocrystals by doping transition-metal ions. ACS Appl Mater Interfaces 2013;5(19):9508–16.
[69] Low WH, et al. One dimensional MnV2O6 nanobelts on graphene as outstanding electrode material for high energy density symmetric supercapacitor. Ceram Int 2021;47(7):9560–8.
[70] Pandiyarajan S, et al. Robust fabrication of silver pyro-vanadates via sonochemical approach for advanced energy storage application. J Alloys Compd 2022;893:162268.
[71] Elkholy AE, Heakal FE-T, Allam NK. A facile electrosynthesis approach of amorphous Mn-Co-Fe ternary hydroxides as binder-free active electrode materials for high-performance supercapacitors. Electrochim Acta 2019;296:59–68.
[72] Instruments G. Basics of electrochemical impedance spectroscopy. In: G. Instruments, complex impedance in corrosion; 2007. p. 1–30.
[73] Noori A, et al. Towards establishing standard performance metrics for batteries, supercapacitors and beyond. Chem Soc Rev 2019;48(5):1272–341.
[74] Kumar RD, Andou Y, Karuppuchamy S. Microwave-assisted synthesis of Zn–WO3 and ZnWO4 for pseudocapacitor applications. J Phys Chem Solid 2016;92:94–9.
[75] Ates M, Arican F, Karazehir T. Electrochemical copolymerization of N-methylpyrrole and 2, 2′-bithitiophene; characterization, micro-capacitor study, and equivalent circuit model evaluation. Bull Mater Sci 2013;36(7):1281–90.
[76] Ates M, Uludag N. Capacitive behaviors and monomer concentration effects of poly (9-benzyl-9H-carbazole) on carbon fiber microelectrode. Fibers Polym 2011;12(3):296–302.
[77] Bredar AR, et al. Electrochemical impedance spectroscopy of metal oxide electrodes for energy applications. ACS Appl Energy Mater 2020;3(1):66–98.

Please cite this article as: Umair M et al., Predominated capacitive behavior of Ag-doped magnesium vanadate as a novel electrode material for supercapacitors, International Journal of Hydrogen Energy, https://doi.org/10.1016/j.ijhydene.2023.05.279